# Appendix A

# Radiation Environment

## A.1 General Features of the Radiation Environment

The nominal luminosity of LHC, $10^{34}$ cm$^{-2}$s$^{-1}$, together with the 7 TeV beam energy, will create a very hostile radiation environment. It has been known since the first LHC feasibility studies, that the inner Tracker of an LHC experiment will have to deal with unprecedented radiation levels. Estimates for the radiation environment expected at the CMS Tracker have been given in several publications over the last years for different assumptions of the Tracker layout and electromagnetic calorimeter material [A-1, A-2, A-3, A-4].

Although radiation damage and high background rates in detectors have become a principal design parameter for the LHC detectors, most of these radiation issues are connected with low energy phenomena, which are the same at almost all existing hadron accelerators. However, at LHC the high beam energy combined with the very high luminosity results in numerous intense cascades, which all end up in an immense number of low energy particles. In fact particle energies exceeding 10 GeV are expected to be very rare in the minimum bias background at $|\eta| < 3$. Therefore the radiation studies, with the exception of a few special cases, have to focus on the energy range around 1 GeV and below. In general, physics simulations evaluating the detector performance do not fully account for all low energy background effects so these have to be addressed in specialized radiation environment simulations.

In the inner parts of the Tracker region the radiation environment is dominated by the secondaries from the pp collisions, but neutron albedo from the surrounding electromagnetic calorimeter starts to dominate at radii larger than about 50 cm.

Starting from a constant particle multiplicity per unit of pseudorapidity ($\eta$) in the central region, it can be shown that the flux in the absence of magnetic fields and material is independent of the $z$-coordinate and varies as $1/r^2$, where $r$ is the distance from the beam-line. The presence of the 4 T magnetic field and the Tracker material cause this $1/r^2$ law not to be exactly obeyed in CMS. However, Fig. A.i demonstrates that the $z$-independence of the flux originating from the vertex is preserved relatively well.

The neutron albedo from the calorimeters leads to an almost uniform neutron flux in the central parts of the tracking volume. Figure A.ii illustrates how this flux increases towards the ECAL endcaps, which are the most intense neutron source in the central CMS detector.

## A.2 Definitions of Radiation Units

Flux is defined as the tracklength of particles per unit of volume per unit of time. For particles arriving at an angle to a flat surface the flux is the number of particles crossing a unit surface per

unit of time, weighted by $1/\cos(\theta)$, where $\theta$ is the angle to the normal of the surface. Fluence is the time integral of flux and is usually expressed in units of $\mathrm{cm}^{-2}$.

Absorbed dose (abbreviated to dose) is the amount of energy deposited per unit of mass and is expressed in Gy (= J/kg).

The component of the radiation field which causes most of the damage depends on the detector type. In particular particle fluence and absorbed dose, although correlated for a given particle type and energy in a given medium, should never be treated as synonyms.

## A.3 Radiation Damage in Silicon

A significant part of LHC related R&D work has concentrated on radiation hardness studies of detectors and electronics. This is especially true for the the silicon detectors to be used in the CMS inner Tracker. Details on different types of damage are given in the relevent detector specific sections. Below, only the aspects important for relating the radiation environment to the damage are described.

### A.3.1 Surface damage

Surface damage is usually the most important damage mechanism for electronics components. It is caused when the charge, generated by the passage of an ionizing particle, gets trapped in the oxide layer. Ionization is by far the dominant energy loss mechanism of charged particles traversing matter. Thus surface damage is a function of the absorbed dose. The latter is a well-defined quantity and arises as a simple number from the radiation simulations. Except for low energy photons, or for hydrogen-containing materials in a radiation environment dominated by neutrons, the material dependence of dose is relatively weak.

### A.3.2 Bulk damage

At the LHC the lifetime of silicon detectors will be limited by bulk damage, which causes an increase of leakage current and changes in the effective doping concentration. The latter effect ultimately leads to very high depletion voltages. Contrary to surface damage, bulk damage depends in a complicated way on the incident particle spectrum. Therefore the use of experimental silicon bulk damage data in order to deduce detector life-expectancies from simulation results, is far more complicated than in the case of surface damage.

All experimental data available at the moment are consistent with the NIEL hypothesis, which states that the bulk damage in silicon has a linear dependence with the non-ionizing energy loss (NIEL) in the silicon. Considerations of cross sections and kinematics show that the NIEL is very small for incident electrons or photons and moderate for muons. It starts to be significant for heavier projectiles, i.e. all hadrons. Since the NIEL is a very small fraction of the total $\mathrm{d}E/\mathrm{d}x$ of a charged particle – and since this fraction is almost zero for electrons – bulk damage has essentially no relationship to radiation dose. Semi-theoretical calculations of the energy and particle type dependence of NIEL [A-5] agree quite well with available experimental data [A-6]. Both the data and the calculations indicate that for the hadron types and energy spectra expected at the LHC the damage in silicon varies by a relatively small factor. The only exception are neutrons for which the damage below 100 keV of energy is practically negligible. Often damage constants are expressed with respect to 1 MeV neutron equivalent fluence. This is a defined quantity, corresponding to a NIEL of 95 MeV mb [A-7]. The LHC spectrum can be averaged with the presently available information of the energy-dependent damage functions to arrive at the average damage constant (= NIEL). The results of such a procedure can be found in Table A.1 for various regions of the CMS Tracker assuming the spectra to be presented

in forthcoming sections. There is a clear tendency for the average NIEL to decrease when the average energy increases, i.e. towards small radii and high pseudorapidities. It should be remembered, however, that due to the lack of consistent experimental data the damage constants are not firmly known over the whole range of LHC energies and particle types. In particular for pions, which dominate the fluence at the inner Tracker layers, experimental data are limited to a narrow energy range around 300 MeV and the calculated values [A-5] are likely to underestimate the NIEL below the $\Delta$-resonance. Thus the values in Table A.1 include significant uncertainties and their relatively small spread around $\sim$95 MeV mb should be taken as an indication that to a good approximation it is sufficient to integrate the flux at LHC over all hadron types and energies (>100 keV for neutrons) and to use the result together with damage constants expressed for 1 MeV neutron equivalent fluence.

Finally, it should be emphasized that Table A.1 and all the associated discussion is valid only for silicon. Even the 100 keV threshold energy for neutrons is a property of silicon. Thus none of these damage arguments should be extended to other materials in a quantitative way.

**Table A.1:** Average NIEL (MeV mb) for the hadron spectra in different parts of the Tracker. The calculations are based on the damage functions given in Ref. [A-5]. The NIEL of 1 MeV neutrons is defined to be 95 MeV mb [A-7]

| | $\|\eta\|$ = 0–0.9 | $\|\eta\|$ =0.9–1.8 | $\|\eta\|$ =1.8–2.7 |
|---|---|---|---|
| $r$ = 0–20 cm | 75 | 69 | 62 |
| $r$ = 20–40 cm | 88 | 85 | 82 |
| $r$ = 40–65 cm | 100 | 95 | 92 |
| $r$ = 65–120 cm | 109 | 106 | 104 |

## A.4 Shielding Requirements and Materials

Inside CMS the shielding is constrained by the very limited space available. Therefore materials have been selected to provide the most efficient shielding in the smallest space. In addition, the shielding strategy must not jeopardize the performance of the detectors through inert material placed in front of them. Both aspects are of utmost importance for the shielding design inside of the ECAL. Most of the neutron flux, which is harmful to the inner Tracker, is generated by hadronic interactions in the ECAL crystals. The choice of the ECAL material significantly affects the neutron albedo; the heavier the elements in the absorber the more albedo [A-1]. In this respect the $PbWO_4$ crystals chosen by CMS are not very favourable. Without any protection, the neutron fluence in the Tracker region would be in the range 5–30 $\times$ $10^{13}$ cm$^{-2}$ for an integrated luminosity of $5 \times 10^5$ pb$^{-1}$ [A-4]. The highest values would occur close to the ECAL endcap and the lowest at a radius of about 50 cm in the centre of the Tracker.

The most efficient method of neutron moderation is based on elastic scattering from hydrogen nuclei. Therefore the main parameter, when trying to minimize thickness, is the hydrogen density per unit of volume. In this respect polyethylene, paraffin and water are almost equivalent. Of these, polyethylene is the easiest to handle and to machine into the desired shape. It also has the advantage of a relatively large radiation length and so does not introduce an unacceptable amount of material in front of the ECAL.

An important consideration is that effective shielding of silicon devices only requires that the neutron energy is lowered below 100 keV. There is no need to absorb the neutrons. Therefore special neutron capture elements like boron or lithium would actually be a disadvantage since they would lower the hydrogen content of pure polyethylene. Similarly, any impregnation or lowering of the average density would reduce the effectiveness of polyethylene.

Most neutrons are produced by evaporation and have an energy around 1 MeV. Owing to the relatively large (n,p) elastic cross section, a few centimetres of polyethylene are sufficient to slow most neutrons below the 100 keV limit. The attenuation of the neutron spectrum produced in the crystals is shown in Fig. A.1 for several neutron energy cut-offs. For the important 100 keV cut-off energy there is no single attenuation length – after a rapid drop during the first centimetres the spectrum becomes increasingly hard and the polyethylene loses its effect. This is due to the fact that the high energy part of the spectrum, which is very weakly attenuated by the polyethylene, starts to form a dominant contribution beyond a thickness of about 10 cm. This suggests that a reasonable thickness for a moderator layer is between a few centimetres and 10 centimetres. Figure A.1 also illustrates the fact that boron-doped polyethylene is a worse moderator than pure polyethylene.

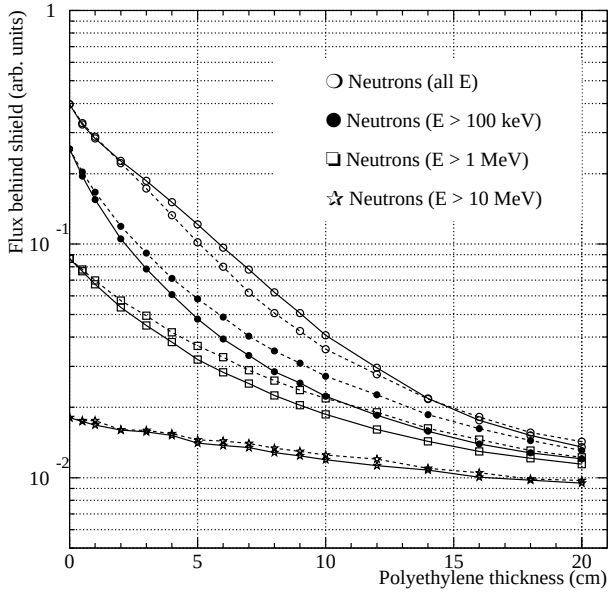


**Fig. A.1:** Simulated neutron flux behind a polyethylene wall, irradiated with the neutron spectrum produced in the ECAL crystals. Each curve shows the integrated flux above the indicated threshold. For silicon, the 100 keV threshold is the significant one. The solid lines correspond to pure polyethylene of density 0.95 g/cm$^3$. The dashed lines are for borated polyethylene of density 0.93 g/cm$^3$.

## A.5 LHC Parameters

### A.5.1 Luminosity

The usually quoted LHC luminosity of $10^{34}$ cm$^{-2}$s$^{-1}$ is in fact the value at the beginning of the fill when the machine is operating at its nominal parameters. During the fill the beam intensity goes down due to various loss processes and the luminosity decreases correspondingly. No final decision on the number of fills per day has been taken, but it has been shown that about the same day-averaged luminosity can be reached with either one or two fills. In both cases this average is roughly half of the nominal value [A-8].

The LHC will not commence with its nominal luminosity but a low-luminosity start-up phase of several years will precede the high luminosity operation. Following the suggestions in Ref. [A-9] we assume that the luminosity during the first year is 10% of the nominal value and rises to 33% in the second year and 67% in the third year. From the fourth year onwards the LHC is assumed to operate at its nominal parameters.

### A.5.2 Assumed operation schedule

Depending on the detector type and the expected radiation effects, either integrated or instantaneous values of fluxes or dose rate are most relevant. Detector occupancies, for instance, depend only on the instantaneous particle rate, whereas radiation damage is often a cumulative effect. For the estimation of induced activity, even differences in the irradiation histories have to be considered. This is because residual nuclides are produced proportionally to the integrated luminosity, but the decay of radioactive isotopes takes place simultaneously and, for a given nuclide, is only a function of time. The time profile of irradiation can also become important for silicon damage, since annealing and reverse annealing are not simple functions of the integrated luminosity, but depend also on the actual time. Therefore an assumption of the machine schedule has to be included in some calculations.

Following the suggestion of [A-9], three periods of 60 days, pp operation per year have been assumed. These periods would be separated by 14-day shutdowns in between. Under these conditions and including a low-luminosity start-up phase, an integrated luminosity of $5 \times 10^5$ pb$^{-1}$ is expected over ten years of LHC operation. This corresponds to $5 \times 10^7$ seconds of operation at LHC peak luminosity.

Heavy-ion operation is foreseen for a relatively short period per year. Tentatively six weeks have been suggested [A-9]. The peak luminosity in the Pb–Pb mode will be $1.95 \times 10^{27}$ cm$^{-2}$s$^{-1}$. Although the inelastic cross section and the average multiplicity in Pb–Pb interactions are expected to be significantly larger than in proton–proton collisions, the average background from Pb–Pb-operation remains about three orders of magnitude below that of the high-luminosity proton–proton collision mode. Thus the heavy-ion operation is not expected to add any significant contribution to the accumulated dose and fluence in detectors and has not been taken into account in the simulations. It should be kept in mind, however, that the instantaneous particle rate and thus the instantaneous energy deposition during a central Pb–Pb collision are expected to be about 50 times higher than during a high-luminosity proton–proton bunch crossing.

## A.6 Induced Radioactivity

While induced radioactivity is negligible at electron–positron colliders, it will be a major concern at the LHC, especially for personnel safety issues. At a hadron accelerator we are confronted with two distinct mechanisms which create remanent radioactivity in materials. These are low-energy neutron interactions [(n,$\gamma$), (n,p), (n,$\alpha$)...] and high-energy hadronic interactions. The former lead from a given target isotope to a well-defined daughter nuclide. The cross sections are, in general, well known up to 20 MeV. Most activation reactions are characterized by thresholds at few MeV and relatively low cross sections. Some materials, however, have very large thermal cross sections for (n,$\gamma$) reactions, which can result in radioactive isotopes. In the Tracker the gold strips of the MSGCs represent a material which is susceptible to neutron activation by (n,$\gamma$) reactions and in the surrounding ECAL the tungsten isotopes will be activated by thermal neutrons.

At energies above 20 MeV we deal with the high-energy regime. Here the final daughter nucleus cannot be deduced from the knowledge of the colliding particles. A high-energy hadronic interaction can, in principle, lead to any residual nuclide with $A$ and $Z$ below those of the target [1]. Nevertheless, peripheral reactions with the removal of only a few nucleons usually dominate, so that most residual nuclei are relatively close to the original target. Roughly 30% of high-energy inelastic hadronic interactions create long-lived radionuclides [A-10, A-11] which contribute to the induced activity dose rate in the experimental area during access periods. This activity

[1] Capture and charge exchange reactions can also lead to $A$ and $Z$ just above those of the target.

decreases relatively slowly after the end of irradiation, so that even long cooling times do not significantly decrease the dose rate.

If the production cross section of a given radionuclide is $\sigma_j$ and the constant irradiation flux is $\phi$, then the activity per unit of volume in a sample after an irradiation time $t_i$ and a cooling time $t_c$ is given by

$$A(t_i, t_c) = \rho \frac{N_A}{M} \sum_j \sigma_j \phi \left[1 - e^{-\lambda_j t_i}\right] e^{-\lambda_j t_c}. \quad \text{(A.1)}$$

Here $\rho$ is the density of the sample, $M$ its molecular mass and $N_A$ is the Avogadro number. The decay constant, $\lambda_j$ is related to the half-life $\tau_j$ by $\lambda = \ln 2/\tau$.

Equation (A.1) does not include the effect of possible cumulative decays, i.e. nuclides decaying into other radionuclides. Equation (A.1) shows that if $t_i \to \infty$, the activity does not increase indefinitely, but approaches a saturation value which is equal to the production rate of radionuclides.

Induced activity is usually regarded as a safety issue only. However, radioactive decays are not taken into account by the simulation codes so the $\gamma$'s and $\beta$'s, which might give an additional contribution to detector background, are not accounted for. In this context it has to be remembered that – contrary to safety issues – even nuclides with very short half-lifes have to be considered.

## A.7 Simulation Methods

### A.7.1 Generation of minimum bias events

The radiation environment simulations are based on minimum-bias events obtained from the DPMJET-II event generator [A-12]. DPMJET-II is the most recent of the Dual Parton Model generators, which are specially suited for simulation of minimum-bias hadronic collisions. As one of the updates with respect to the older DTUJET93 [A-13] program, DPMJET-II includes a complete description of charm production. The high-$p_{\mathrm{T}}$ physics has been further complemented by adding a proper fraction of pure b-events from PYTHIA [A-14] to the DPMJET-II events. Differences between DPMJET-II and DTUJET93 event sets are mainly in high-$p_{\mathrm{T}}$ and diffractive events. As far as the Tracker is concerned both generators give very similar results.

Figure A.2 shows the charged multiplicity and transverse momentum distribution for the DPMJET-II events and, for comparison, minimum-bias events obtained from PYTHIA 5.7. When comparing the distributions from the two event generators it should be noted that the multiplicity is not independent of the assumed cross section. In particular the PYTHIA multiplicity decreases if the cross section is forced to increase [A-2]. The DMPJET-II events, which include single diffraction, correspond to 80 mb inelastic cross section, whereas the inelastic cross section corresponding to the PYTHIA events is only 65 mb. Thus, even though the multiplicity per event is higher with PYTHIA, the average multiplicity per unit of time is lower than with DPMJET-II.

The global scaling parameter for the radiation levels at LHC is the inelastic interaction rate, which is the product of the luminosity and the inelastic cross section. For the latter a value of 80 mb will be assumed. This includes a sizeable fraction of diffractive events. Some 15% of the collisions are expected to be single diffractive. In these events one participating proton continues with only a small transverse deflection, as in elastic scattering and only the dissociated proton contributes to the radiation background in the experimental area. Double diffraction is a relatively rare process and as far as the radiation environment is concerned it will be essentially equivalent to normal inelastic collisions.

To understand broadly how energy is distributed in the experimental area, the angular distributions of the particles emerging from the generated minimum-bias events are analysed.

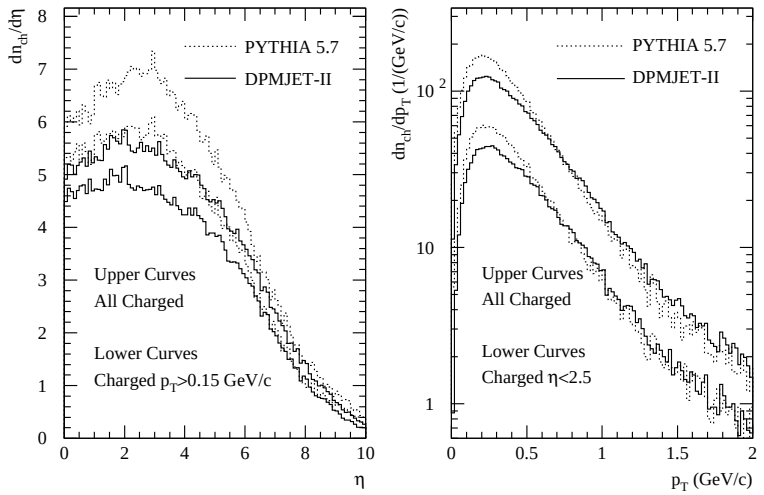


**Fig. A.2:** Charged particle multiplicities as a function of pseudorapidity and transverse momentum according to DPMJET-II and PYTHIA 5.7 event generators. The differences are compensated by the corresponding cross sections which are 80 mb and 65 mb, respectively.

Table A.2 shows the average total energy distribution into different $\eta$ regions, obtained with DPMJET-II.

The DPMJET-II minimum-bias event file used for the simulations includes 2000 events. For the radiation studies the 25 ns bunch structure of the LHC is not significant and even the correlations within a single event can be neglected. This allows for both files to be randomized, i.e. the secondaries were randomly reordered resulting in a smoother source at the cost of destroying the event structure. The average total multiplicity per event is used to scale the simulation results to the proper luminosity.

**Table A.2:** Average energy distribution of one inelastic minimum-bias event into different pseudorapidity regions according to predictions from the DPMJET-II event generator. The values represent a sum of both sides of the detector. The magnetic field and particle decays are neglected

| $\eta$ = 0.0–3.0<br>Central detector | $\eta$ =3.0–5.3<br>Forward calorimeters | $\eta$ =5.3–7.8<br>Collimators | $\eta$ >7.8<br>Leaving area |
|---|---|---|---|
| 100 GeV | 760 GeV | 4200 GeV | 8900 GeV |

## A.7.2 Radiation transport codes

The radiation simulations are independent of the general detector simulations and are performed with the FLUKA [A-15] simulation code, which is specially designed for radiation physics.

FLUKA has a full treatment of high-energy physics, but special emphasis has been put on effects occurring around energies of a few GeV and below. The main FLUKA features, which are important for the radiation environment simulations at the CMS Tracker are:

- generation of hadronic interactions from thermal neutrons up to 20 TeV,
- pre-equilibrium cascade model for inelastic interactions below 1.3 GeV and for capture reactions at rest,
- nuclear evaporation and gamma de-excitation after inelastic interactions,
- extended version of the EGS4 electromagnetic shower code [A-16, A-17],
- multigroup transport of neutrons below 20 MeV with detailed kinematics for (n,p) scattering and accounting for self shielding effects in some materials,
- neutron capture reactions with explicit photon emission,

- accurate multiple scattering and magnetic field transport even in thin layers,
- full accounting for ionization loss, including explicit $\delta$-electron production and latest parametrizations for the density effect at high energies and shell corrections at low energies.

### A.7.3 General geometry description

A substantial effort has been devoted to finding the best parameters and approximations to describe the CMS system so that it remains feasible to implement with the relatively unsophisticated geometry routines of FLUKA. Roughly 2000 volumes are needed to achieve this for the full CMS detector including shielding, the surrounding hall and the V4 Tracker version. Each detector has been described with the minimum accuracy which was considered sufficient. For the Tracker this means that a quite rough description for the outer detector parts is sufficient whereas the Tracker itself has to be described in sufficient detail to reproduce mass distributions properly.

A major approximation is that everything is assumed to have cylindrical symmetry. This is enforced by the fact that azimuthal averaging has to be applied in order to obtain results with sufficient statistics.

Since outer parts of the CMS detector and the experimental cavern have negligible impact of the radiation field within the central detector the cascade development in them has been disfavoured with the powerful biasing techniques available in FLUKA. By reducing the amount of CPU time per particle this allows better statistics to be collected in the Tracker region, while preserving possible effects due to external elements, in particular the forward calorimeter.

### A.7.4 Energy cuts and transport parameters

The lower threshold for neutron transport was set to thermal energy at 293 K. Although the thermal neutron group of FLUKA ranges from $10^{-5}$ eV to 0.414 eV, the cross sections in the 293 K group correspond to a mean thermal neutron energy of 0.025 eV. The transport cut for charged hadrons was set to 10 keV. Antineutron transport was stopped at 50 MeV, which is dictated by available cross section data. Energy cuts for electromagnetic particles are more problematic because of the intolerable increase of computing time if cuts are set too low. Therefore the energy thresholds for photon, electron, and positron transport were adjusted according to the region. The absolute lower cut was 100 keV for electrons and 30 keV for photons, which was used in all detectors directly visible from the Tracker. In outer regions these cuts were raised considerably in order to save CPU time. At the cuts the action of the simulation code depends on the type of particle. For electromagnetic particles the energy is deposited on the spot but the photons emitted in positron annihilation are further transported. Other charged particles are ranged out to rest and, if applicable, capture on a nucleus is enforced. Neutral particles are transported until they decay or get captured. Antineutrons falling below the threshold are forced to interact after having travelled a distance corresponding to the cross section at threshold.

The full 2-dimensional (azimuthally symmetric) magnetic field map of CMS was used in the region of the central detector.

Multiple scattering was performed down to the Molière limit. Delta electrons were produced above 100 keV. Pair production and bremsstrahlung were explicitly simulated for high-energy muons and charged hadrons.

### A.7.5 Scoring

The particle fluxes have been obtained by using a tracklength estimator in the the detector layers. For silicon the scoring was done in 600 $\mu$m thick silicon plates, representing the sensitive volume and part of the averaged services and electronics, and for the MSGCs in 3 mm wide gas gaps. All charged hadrons and neutral kaons have been grouped together. The antineutron fluence, significant only at the pixel detectors, has been combined with the neutron fluence.

The dose has been obtained as total energy deposition in the silicon plates or the glass substrates of the MSGCs.

For a detailed estimation of radiation damage and activation issues the energy spectra of the particles are indispensable. These have been obtained in 9 regions limited by radii of 20 cm, 65 cm and 120 cm and $\eta$-lines of 0.9, 1.8 and 2.7. In these regions the spectra were scored as tracklength in the detector elements.

### A.7.6 Estimation of error margins

All simulations have been divided into several independent batches of equal size. These have been used to estimate the statistical errors arising from fluctuations in the event sampling and during cascade simulation. In the figures only these statistical error estimates are indicated, as 1 $\sigma$ error bars. Systematic errors are usually more important.

Uncertainties arise from the extrapolation of existing data to the inelastic proton–proton cross section at 14 TeV as well as from the estimates of event multiplicities and momentum distributions of the minimum-bias events. These lead to an underlying uncertainty of about 30% from the pp events alone [A-2] which probably cannot be reduced before LHC minimum-bias data is available. This error is the dominant one as far as charged hadron fluxes in the CMS Tracker are concerned. Table A.3 shows the longitudinally averaged hadron and neutron fluences at some layers of the barrel Tracker for three different event generators. The cross section suggested by PYTHIA, single diffraction excluded, is 65 mb. For DTUJET93 and DPMJET-II a cross section of 80 mb was used. Both of the latter include single diffractive events. We can observe very good agreement between the results obtained from these three event generators. Although DPMJET-II and DTUJET93 are to a large part the same code, PYTHIA differs from these substantially. Thus the good agreement gives some confidence in the extrapolation of minimum-bias event generation to $\sqrt{s}$ = 14 TeV. Although the difference between the three event generators compared is small, some other models – like the one used for the Technical Proposal – give higher fluences, which justifies the use of an error bound, as large as 30%, for the charged particle fluences.

For particles other than the pp secondaries, uncertainties in the cascade development dominate. The accuracy of the cascade simulation is affected by approximations in the geometry description and incompleteness of physics models and cross section data sets.

**Table A.3:** Longitudinally averaged particle fluxes ($10^6 \mathrm{cm}^{-2}\mathrm{s}^{-1}$ at LHC peak luminosity) at some layers of the barrel Tracker for three different event generators

| Radius | Particle type | DPMJET-II | DTUJET93 | PYTHIA5.7 |
|---|---|---|---|---|
| 7.1 cm | Ch. hadron & $K^0$ | 17.5±0.01 | 17.9±0.02 | 15.4±0.02 |
| | Neutron ($E$ >100 keV) | 2.16±0.02 | 2.08±0.07 | 1.55±0.08 |
| 22 cm | Ch. hadron & $K^0$ | 2.41±0.03 | 2.58±0.04 | 2.23±0.08 |
| | Neutron ($E$ >100 keV) | 0.69±0.02 | 0.70±0.02 | 0.64±0.05 |
| 98.5 cm | Ch. hadron & $K^0$ | 0.08±0.00 | 0.08±0.00 | 0.07±0.01 |
| | Neutron ($E$ >100 keV) | 0.23±0.00 | 0.24±0.01 | 0.18±0.00 |

FLUKA has been benchmarked in several small scale experiments using neutron counters and activation foils. The agreement with measurements is of the order of few tens of per cent even after several attenuation lengths of shielding [A-18]. Nevertheless these relatively simple experiments cannot be guaranteed to give a reliable error bound for the case of the neutron albedo from the CMS ECAL, which is dominated mainly by the accuracy with which the neutron production in hadronic collisions is described. This is hadron physics around a few GeV which is a difficult domain for Monte Carlo modelling, because of a mixing of nuclear structure and high-energy effects. Intercomparisons between different Monte Carlo models for the CMS ECAL suggest that an uncertainty of a factor of 2 should be expected in the neutron albedo.

Since the charged hadron flux dominates in the most exposed part of the silicon Tracker, a total safety factor of about 1.5 should be applied to the fluences presented in the following sections. For the pixel detector this factor could be reduced slightly but correspondingly it should be increased in regions dominated by the neutron albedo.

The induced activity calculations are a special case. The uncertainties in the cascade simulation are negligible compared to those of the radionuclide production cross sections or residual nuclei yields as given by the simulation codes. In addition the geometries and material distributions used for the calculations involve quite significant approximations. The reader should not be misled by the number of digits with which data are given in plots and tables. Usually the accuracy is introduced only to indicate local variations of the values, i.e. relative differences. The absolute values given by the induced activity calculations should not be assumed to be accurate to better than a factor of about 5, although in some special cases a better accuracy can be achieved. Thus the induced activity dose rates and particle fluxes should be interpreted merely as indicators of the order of magnitude.

### A.7.7 Simulation of LHC beam losses

It can be expected that for the Tracker the worst beam loss condition would be if beam particles, heading towards the experiment, would be lost in the low-$\beta$ section or on the copper collimator. With its $r = 17$ mm aperture the collimator serves as an efficient protection against losses in the experiment itself.

Loss patterns or probabilities of such events have not yet been provided by the LHC machine experts. A study of realistic loss patterns and accidental loss conditions has been initiated within CMS and a preliminary indication is that some accidental conditions could lead to a loss of a significant fraction of the full beam in the low-$\beta$ section. No indication has been found so far that losses could happen directly on the collimator.

Since these studies are in a preliminary stage and also require cross-checking by the LHC machine experts, we prefer to do a simplified case study by simulating beam losses on the collimator. Although this will be pessimistic with respect to losses further upstream, it serves the purpose of giving an indication of how a beam loss close to the experiment is reflected at the Tracker. Before more detailed studies are ready, we do not make any statement about the possible loss rates but normalize all results to one proton incident on the collimator.

A proton could hit the collimator either at the end or at grazing angle at the inner aperture. The latter can be expected to be more dangerous, since grazing protons would not see the full attenuation length of the collimator. Beam losses were simulated by shooting 7 TeV protons at the back end of the collimator, uniformly distributed between radii of 16 mm and 18 mm and having an angle of 60 $\mu$rad to the beam axis. Secondaries were transported through the collimator, the shielding, and the forward calorimeter and fluences and radiation dose were scored in the inner Tracker.

### A.7.8 Estimation of induced radioactivity

The residual nuclide yield in high-energy interactions is difficult to estimate, since experimental cross sections are only rarely available for the particle, target, energy combinations of interest [A-19]. Some extrapolations of available data are possible, but the associated uncertainties are significant. The hadronic event generators of some simulation codes, like FLUKA, can be used directly to estimate the residual nuclide yields. But although the interaction models have improved over the last years, there are still significant uncertainties, especially concerning the residual nuclei.

If we consider safety aspects, we can neglect all nuclei with very short half-lifes, since these will have disappeared after a reasonably short cooling time. Thus it is often relatively easy to explicitly identify the nuclides which need to be considered in a safety analysis. This is true, especially, for light target materials ($A$ <30), where the most important radioisotopes are $^{7}$Be, $^{22}$Na and $^{24}$Na. The experimental cross sections can be used together with the fluxes from the simulations to arrive at production rates of individual radionuclides. For the Tracker this procedure has been followed with cross sections for aluminium and iron and results are reported in Section 6.9.8.

The situation becomes much more complicated if we consider increased rates in detectors during operation. In this case none of the short-lived nuclides can be excluded. Experimental data on production rates of such more exotic nuclei is too incomplete to be useful. So the only way to estimate this effect is to use the hadronic event generators to obtain the production cross sections. In addition chain decays are very common for such short-lived nuclides. Thus Eq. (A.1) is not valid and the decay chains have to be followed explicitly. We use the DeTra code [A-20] for this task. This code allows one to calculate analytically the decay chains of some 4400 nuclides in its database and to extract the explicit photon and $\beta$-spectra at any instant of time during an arbitrary irradiation/cooling cycle.

The estimation of detector background requires an accounting for induced activity in the Tracker itself, but also in the beam pipe and the surrounding ECAL. These activaties have been determined from results of FLUKA simulations. The time dependence is followed with the DeTra code and the induced activity photons are transported in the Tracker geometry using FLUKA. More details on the simulations can be found in Ref. [A-21].

## A.8 Pixel Detector

The pixel detector is located closest to the interaction point where the radiation environment is dominated by the pp secondaries directly. The particle fluences and radiation dose at the three barrel layers and the two forward disks can be found in Fig. A.3. We can observe a very strong radial dependence of the charged particle fluence and a less pronounced variation of the neutron fluence. In both cases the variation along the $z$-axis is small. The dose follows roughly the behaviour of the charged hadron fluence.

The independence on the $z$-coordinate allows fluences over $z$ to be averaged in order to arrive at characteristic values for each radial layer. The averaged results are given in Table A.4, which also shows the proportion of different hadron types. For the relatively compact pixel detector these averaged data are directly applicable to the endcap disks at the corresponding radius.

Figure A.4 demonstrates how all spectra become harder towards higher pseudorapidity and that the charged hadron fluence is dominated by pions with protons and charged kaons each accounting for about 10%. The maximum of the spectrum occurs between 400 MeV and 2 GeV depending on the $\eta$-range considered.

The photon spectrum shows a high-energy component due to $\pi^0$ decays and a significant flux of low energy photons which is mainly produced by neutron capture and nuclear de-excitation.

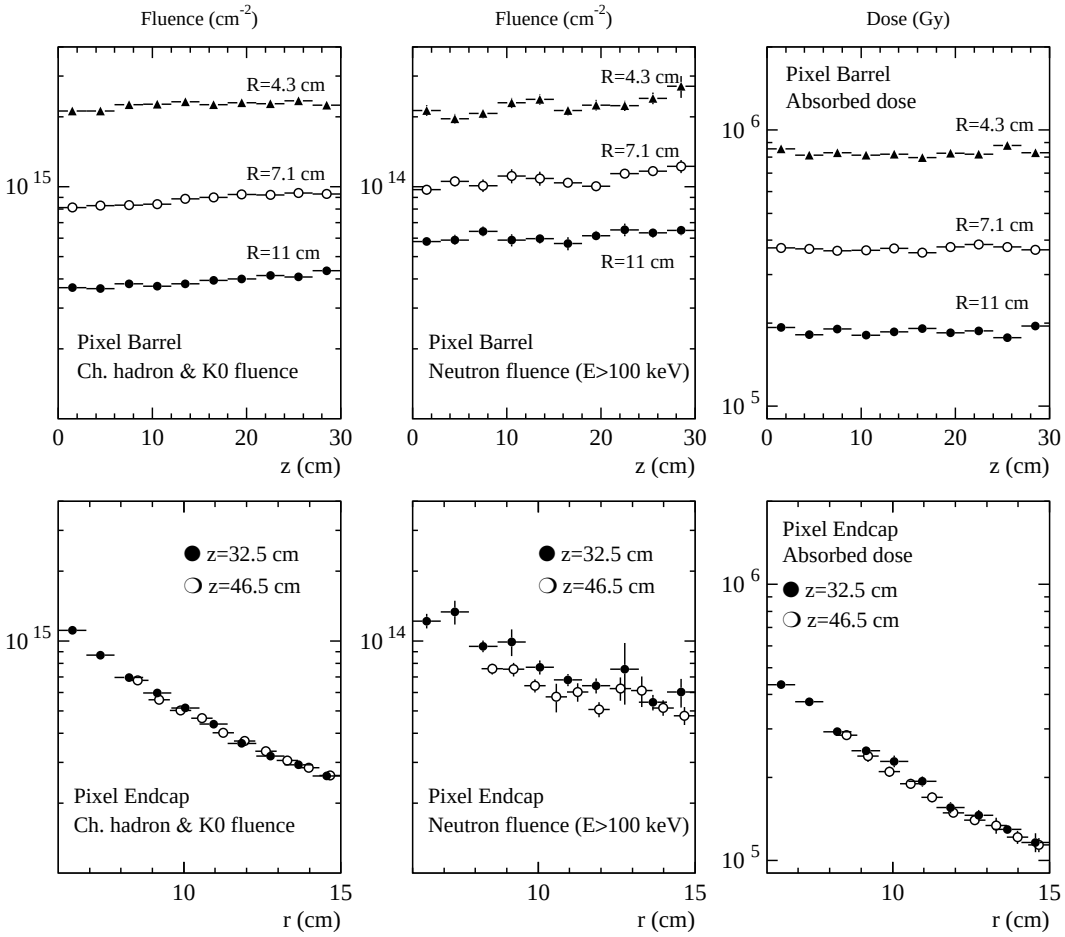


**Fig. A.3:** Energy-integrated charged hadron and neutron fluences and absorbed dose in the pixel detector. All values are for an integrated luminosity of $5 \times 10^5$ pb$^{-1}$.

**Table A.4:** Longitudinally averaged hadron fluences in the three layers of the barrel pixel detector. All fluence values are given as $10^{13}$ cm$^{-2}$ for an integrated luminosity of $5 \times 10^5$ pb$^{-1}$. The fast hadron fluence is the sum over the first five rows of each column and serves as a good approximation to the 1 MeV equivalent fluence. The indicated errors refer to the simulation statistics only

| | 4.3 cm | 7.1 cm | 11 cm |
|---|---|---|---|
| Charged pions | 180±1 | 71.8±0.3 | 32.6±0.2 |
| Protons | 15.5±0.2 | 6.1±0.1 | 2.66±0.07 |
| Charged kaons | 17.3±0.2 | 6.2±0.1 | 2.48±0.04 |
| Neutral kaons | 11.0±0.2 | 3.60±0.08 | 1.33±0.03 |
| Neutrons ($E$ >100 keV) | 22.6±0.4 | 10.8±0.2 | 6.11±0.1 |
| Thermal neutrons | 5.6 ±0.5 | 5.0±0.2 | 5.2±0.2 |
| Neutrons total | 29.2±0.6 | 16.8±0.3 | 12.3±0.2 |
| Fast hadrons | 246±1 | 98.5±0.4 | 45.2±0.2 |
| Absorbed dose (kGy) | 828±7 | 371±4 | 187±2 |

The neutron spectrum at the pixel detector is remarkably hard in all three $\eta$-regions, but especially at the higher $\eta$-values. This indicates that the majority of the neutrons are secondaries emerging from the pp collision.

The pixel optical link transmitters will also be situated close to the interaction point. In order to estimate the radiation levels at their location the dose and particle fluences have been simulated for a cylinder of radius 18.7 cm extending from $z = 32.6$ cm to $z = 46.6$ cm. The

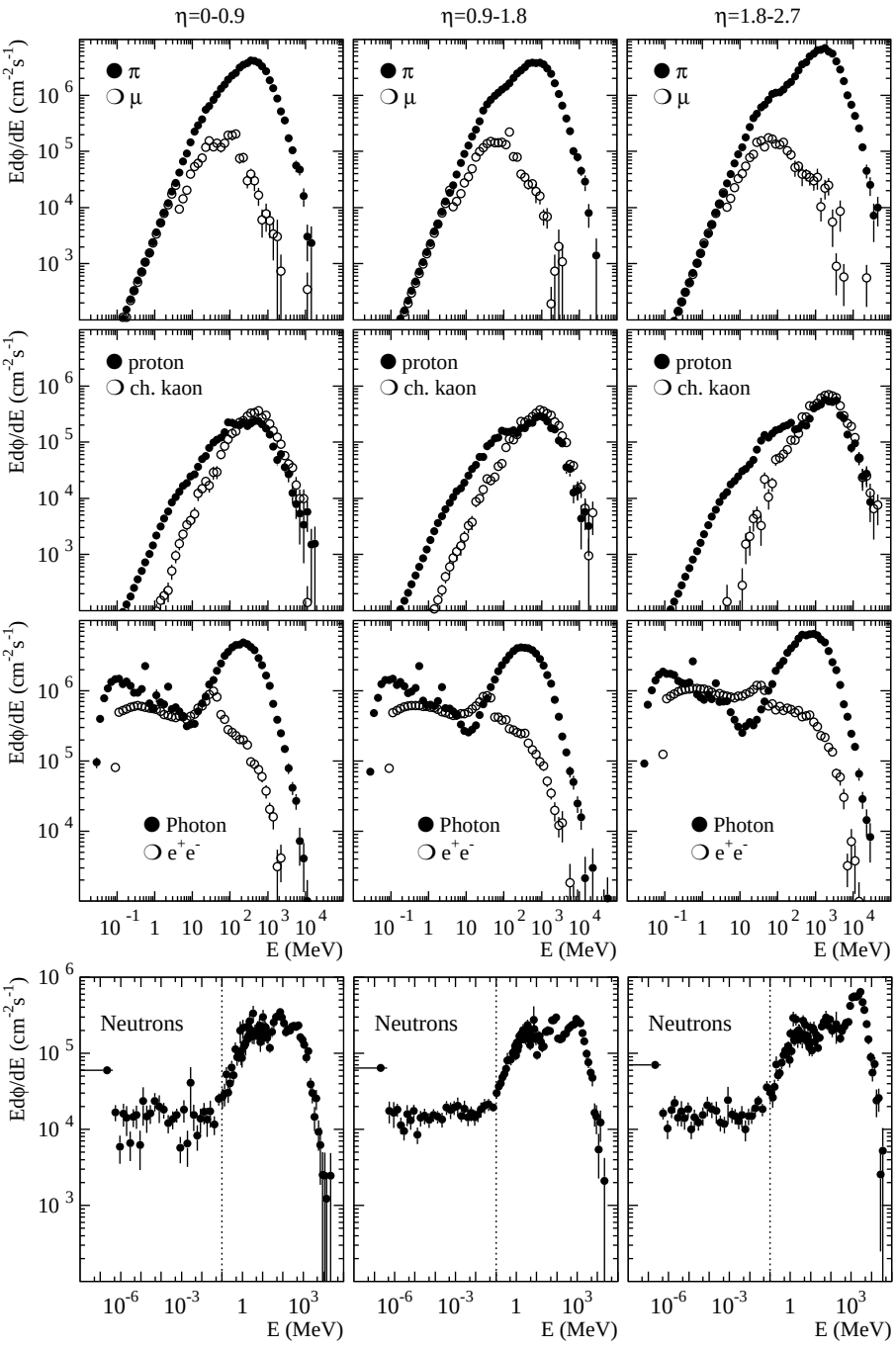


**Fig. A.4:** Energy spectra of the most important particles types in the pixel detector. The vertical line indicates the critical 100 keV limit for neutrons. All values are for a luminosity of $10^{34}$ cm$^{-2}$s$^{-1}$.

radiation dose is 80±2 kGy, the charged hadron fluence is (1.69±0.03)×$10^{14}$ cm$^{-2}$ and the neutron fluence above 100 keV is (4.0±0.2)×$10^{13}$ cm$^{-2}$. The optical links will not be silicon devices hence the 100 keV cut applied on neutrons may not be approppriate and the corresponding fluence should only be taken as an indicative value [A-22]. Since, however, the fluence between 100 keV and the thermal regime is only 1×$10^{13}$ cm$^{-2}$, the neutron fluence shown with the 100 keV cutoff should not be too optimistic by more than 25%.

## A.9 Silicon Tracker

The silicon Tracker extends from an inner radius of just over 20 cm to about 60 cm. Along the $z$-axis it spans the whole length of the Tracker. The barrel detector consists of five concentric layers. Each endcap has 10 disks distributed along the available space in $z$. Figure A.5 shows the charged hadron and neutron fluences and the radiation dose at the barrel layers and some endcap disks. Like for the pixel detector there is a relatively strong radial variation but only weak $z$-dependence of the charged hadron fluences. The neutron fluence shows a clear increase at the endcap disks closest to the ECAL. The radial variation of the neutron fluence is relatively small, the excess at small radii being due to the neutron and antineutron fluence from the vertex.

The longitudinally averaged values for the barrel Tracker are given in Table A.5. As can be concluded from Fig. A.5 the neutron fluence, especially, increases towards the endcap ECAL. Even the charged fluence increases slightly with the $z$-coordinate in the most exposed $r = 22$ cm layer. Thus the average fluence of $(1.57 \pm 0.01) \times 10^{14}$ cm$^{-2}$ given in Table A.5 is pessimistic for $z = 0$ (actual fluence $(1.50 \pm 0.03) \times 10^{14}$ cm$^{-2}$) and optimistic for $z = 48$ cm (actual fluence $(1.66 \pm 0.03) \times 10^{14}$ cm$^{-2}$).

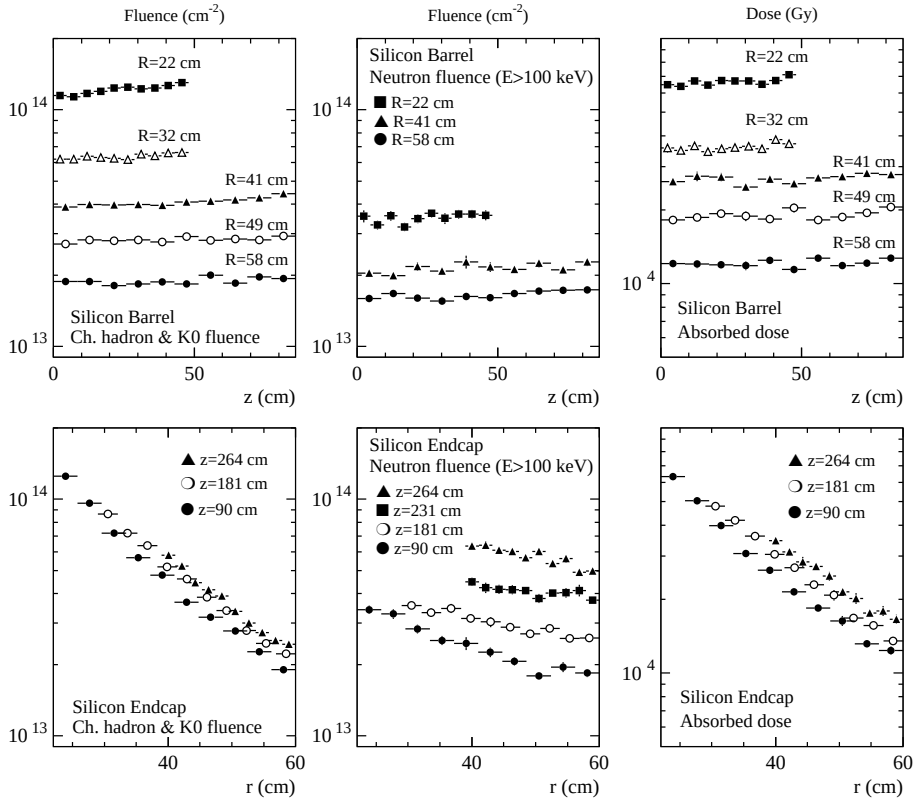


**Fig. A.5:** Energy-integrated charged hadron and neutron fluences and absorbed dose in the silicon Tracker. All values are for an integrated luminosity of $5 \times 10^5$ pb$^{-1}$. For the endcap disks it should be noted that values are averages over the indicated radial range.

Correspondingly, an extrapolation of the barrel averages to the endcap disks is not exactly justified for the silicon Tracker. Since the radial variation is significant over the 4 cm wide bins used for the scoring in the endcap disks, the data shown in Fig. A.5 do not reproduce the fluence maxima accurately. A finer binning together with a suitable interpolation has been used to deduce these values for the low edges of the endcap disks. The values obtained are listed in Table A.6. The most exposed point in the silicon Tracker is at the low edge of the sixth endcap disk, where the fast hadron fluence reaches $(1.91 \pm 0.02) \times 10^{14}$ cm$^{-2}$.

A comparison with the CMS Technical Proposal shows that the fluence and dose values presented now are systematically lower. The main part of the reduction arises from the use of latest event generators which include most recent parton structure functions and thus give lower particle multiplicities than the DTUJET92 generator used for the Technical Proposal [A-2]. Also the assumption of 80 mb inelastic non-diffractive cross section in the Technical Proposal has been corrected to about 67 mb[2] to bring it in agreement with generally agreed extrapolations.

**Table A.5:** Longitudinally averaged hadron fluences and absorbed dose in the five layers of the barrel silicon Tracker. All values are given as $10^{13}$ cm$^{-2}$ for an integrated luminosity of $5\times10^5$ pb$^{-1}$. The fast hadron fluence is the sum over the first five rows of each column and serves as a good approximation to the 1 MeV neutron equivalent fluence. The indicated errors refer only to the simulation statistics

| | 22 cm | 32 cm | 41 cm | 49 cm | 58 cm |
|---|---|---|---|---|---|
| Charged pions | 10.3±0.1 | 5.39±0.07 | 3.40±0.04 | 2.33±0.03 | 1.53±0.03 |
| Protons | 0.96±0.02 | 0.54±0.01 | 0.41±0.01 | 0.31±0.01 | 0.235±0.004 |
| Charged kaons | 0.61±0.01 | 0.28±0.01 | 0.177±0.005 | 0.125±0.003 | 0.087±0.003 |
| Neutral kaons | 0.30±0.01 | 0.128±0.004 | 0.08±0.00 | 0.053±0.001 | 0.038±0.001 |
| Neutrons ($E$ >100 keV) | 3.50±0.07 | 2.54±0.05 | 2.15±0.03 | 1.85±0.03 | 1.65±0.02 |
| Thermal neutrons | 5.0±0.1 | 5.1±0.1 | 5.15±0.09 | 5.08±0.08 | 5.09±0.09 |
| Neutrons total | 9.5±0.1 | 8.5±0.1 | 8.3±0.1 | 7.9±0.1 | 7.7±0.1 |
| Fast hadrons | 15.7±0.1 | 8.88±0.09 | 6.22±0.05 | 4.67±0.04 | 3.54±0.04 |
| Absorbed dose (kGy) | 66.6±0.6 | 36.1±0.5 | 26.9±0.4 | 19.1±0.3 | 12.1±0.2 |

**Table A.6:** Hadron fluences at the lowest edges of some silicon endcap disks. All values are given as $10^{13}$ cm$^{-2}$ for an integrated luminosity of $5\times10^5$ pb$^{-1}$. The fast hadron fluence is the sum over the first five rows of each column and serves as a good approximation to the 1 MeV neutron equivalent fluence. The indicated errors refer to the simulation statistics only

| $z$-coordinate (cm) | 90 | 128 | 162 | 206 | 264 |
|---|---|---|---|---|---|
| Radius (cm) | 22 cm | 22 | 22 | 29 | 39 cm |
| Charged pions | 11.7±0.1 | 11.9±0.2 | 12.6±0.2 | 7.8±0.2 | 4.6±0.1 |
| Protons | 1.09±0.05 | 1.20±0.05 | 1.29±0.06 | 0.97±0.04 | 0.75±0.04 |
| Charged kaons | 0.69±0.04 | 0.76±0.03 | 0.80±0.03 | 0.48±0.03 | 0.24±0.02 |
| Neutral kaons | 0.42±0.03 | 0.35±0.02 | 0.34±0.02 | 0.17±0.02 | 0.11±0.01 |
| Neutrons ($E$ >100 keV) | 3.6±0.1 | 3.4±0.1 | 4.1±0.1 | 3.9±0.1 | 6.4±0.2 |
| Fast hadrons | 17.5±0.2 | 17.6±0.2 | 19.1±0.2 | 13.3±0.2 | 12.1±0.2 |

It can be seen from Fig. A.5 that charged hadrons dominate the fluence at all radii in the barrel. In the forward region the situation is different; because of the intense albedo from the endcap ECAL the neutron fluence at the last disks clearly exceeds the charged hadron fluence. Thus the fluence at these disks is dominated by albedo neutrons and the importance of moderators around the ECAL should not be underestimated. The present layout foresees a total of 8 cm high-density ($\rho = 0.95$ g/cm$^3$) polyethylene at the endcap. Previous simulations [A-4] have shown that the neutron fluence at the last Tracker endcap disks would increase by a factor of about 2 if the moderator thickness would be halved and by a factor of 5 if the moderator would be completely removed.

The energy spectra of most important particles are shown in Fig. A.6. The strong dominance of charged pions is clearly illustrated. The neutron spectrum is not as hard as at the pixel detector and the typical evaporation peak at about 1 MeV and the quasi-elastic peak at 70 MeV are distinguishable. The photon spectrum is dominated by photons below 10 MeV.

[2]We assume 80 mb but include diffractive events, leaving a non-diffractive cross section of about 67 mb.

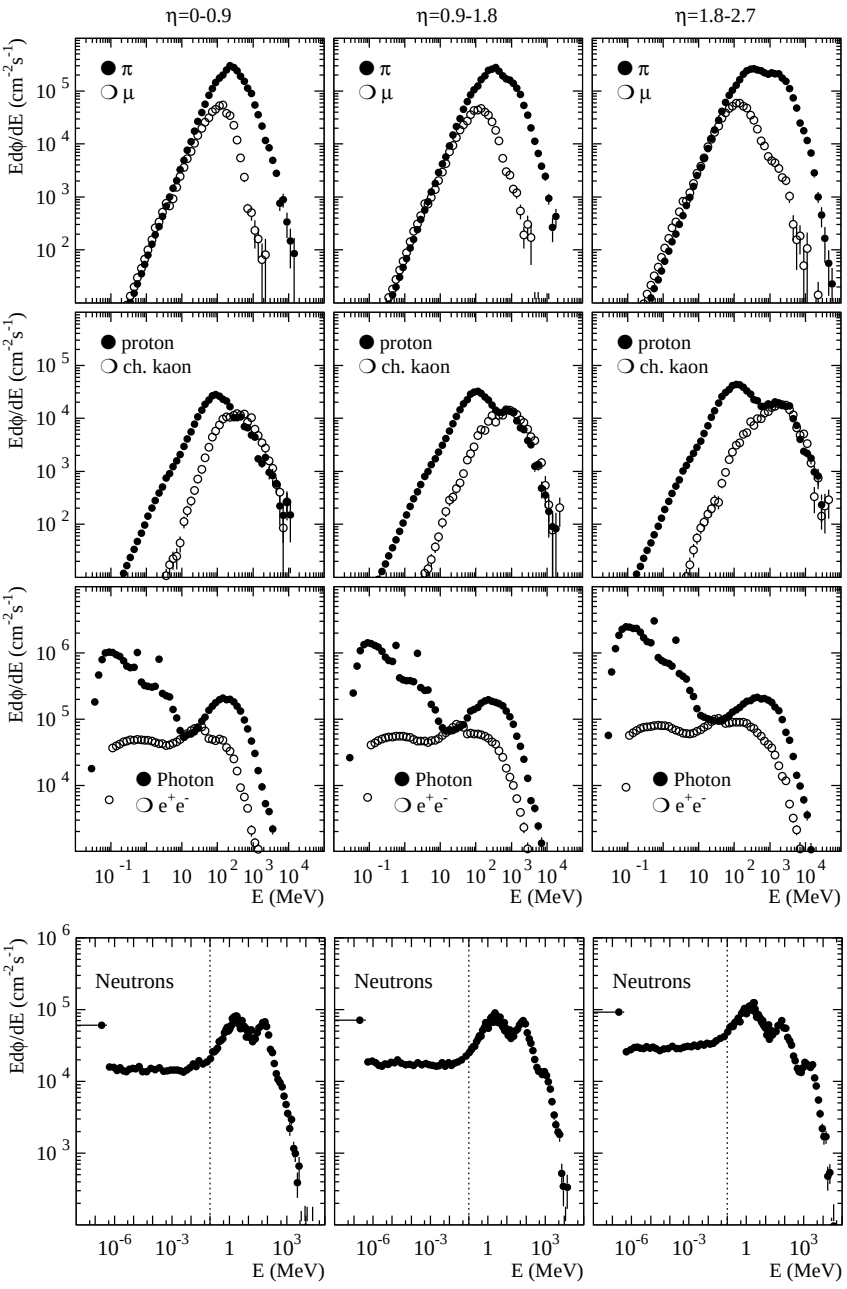


**Fig. A.6:** Energy spectra of the most important particles types in the silicon Tracker. The vertical line indicates the critical 100 keV limit for neutrons. All values are for a luminosity of $10^{34}$ cm$^{-2}$s$^{-1}$.

## A.10 MSGC Tracker

The outermost layer of the CMS tracking system is formed by the MSGC Tracker. The MSGCs are gas detectors with a 3 mm gas gap enclosed between a glass substrate and a drift plane. Thus the MSGC detectors themselves do not suffer from bulk damage like the silicon detectors. But the readout electronics is similar to the silicon Tracker and will be susceptible to radiation damage. For the electronics the absorbed dose should be most significant, but for completeness also the charged particle and neutron fluences in the MSGC gas gaps are shown in Fig. A.7. The absorbed dose, shown in Fig. A.7, corresponds to energy deposition in the glass substrate which is a good representation of the electronics chips.

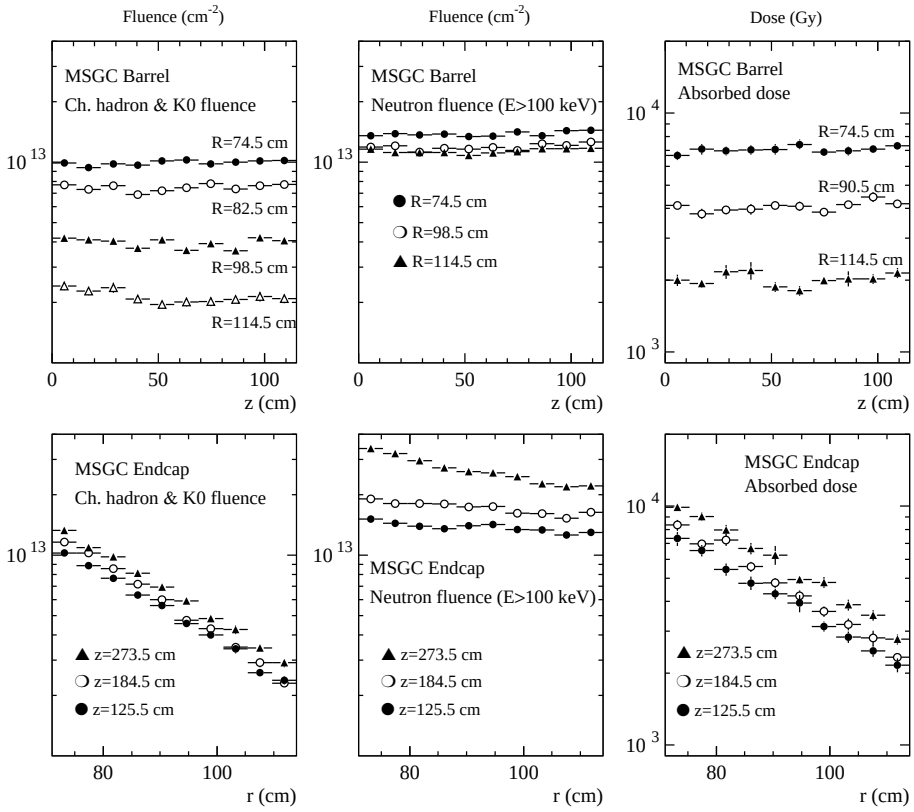


**Fig. A.7:** Energy-integrated charged hadron and neutrons fluences and absorbed dose in the MSGC Tracker. All values are for an integrated luminosity of $5 \times 10^5$ pb$^{-1}$.

The longitudinally averaged values for the barrel detector can be found in Table A.7. We can conclude from Fig. A.7 that the neutron fluence increases slightly at the last endcap disks whereas the charged hadron fluence and the dose are essentially independent of the $z$-coordinate. Thus an extension of the barrel averages into the endcap is valid, except for the neutron fluences at the last disks.

The particle spectra are especially important for the MSGCs, since secondary effects, like highly ionizing particle rates can be estimated only from detailed information of energy and particle type. These data are given in Fig. A.8. Also the thermal neutron fluence, given in Table A.7 has a special role for the MSGCs, because the gold strips have a thermal neutron activation cross section of $10^5$ mb.

**Table A.7:** Longitudinally averaged hadrons fluences in five layers of the barrel MSGC Tracker. All values are given as $10^{13}$ cm$^{-2}$ for an integrated luminosity of $5 \times 10^5$ pb$^{-1}$. The indicated errors refer to the simulation statistics only

| | 74.5 cm | 82.5 cm | 90.5 cm | 98.5 cm | 114.5 cm |
|---|---|---|---|---|---|
| Charged pions | 0.78±0.01 | 0.576±0.009 | 0.420±0.007 | 0.290±0.005 | 0.151±0.004 |
| Protons | 0.142±0.004 | 0.117±0.003 | 0.086±0.002 | 0.070±0.002 | 0.042±0.002 |
| Charged kaons | 0.050±0.002 | 0.037±0.002 | 0.030±0.001 | 0.024±0.001 | 0.013±0.001 |
| Neutral kaons | 0.022±0.001 | 0.018±0.001 | 0.015±0.000 | 0.012±0.000 | 0.008±0.000 |
| Neutrons ($E > 100$ keV) | 1.38±0.02 | 1.30±0.01 | 1.24±0.01 | 1.19±0.01 | 1.13±0.01 |
| Thermal neutrons | 5.00±0.06 | 4.89±0.07 | 4.85±0.07 | 4.77±0.06 | 4.57±0.06 |
| Neutrons total | 7.31±0.08 | 7.13±0.09 | 7.04±0.09 | 6.91±0.09 | 6.68±0.08 |
| Absorbed dose (kGy) | 7.0±0.1 | 5.3 ±0.1 | 4.06±0.07 | 3.32±0.06 | 2.03±0.05 |

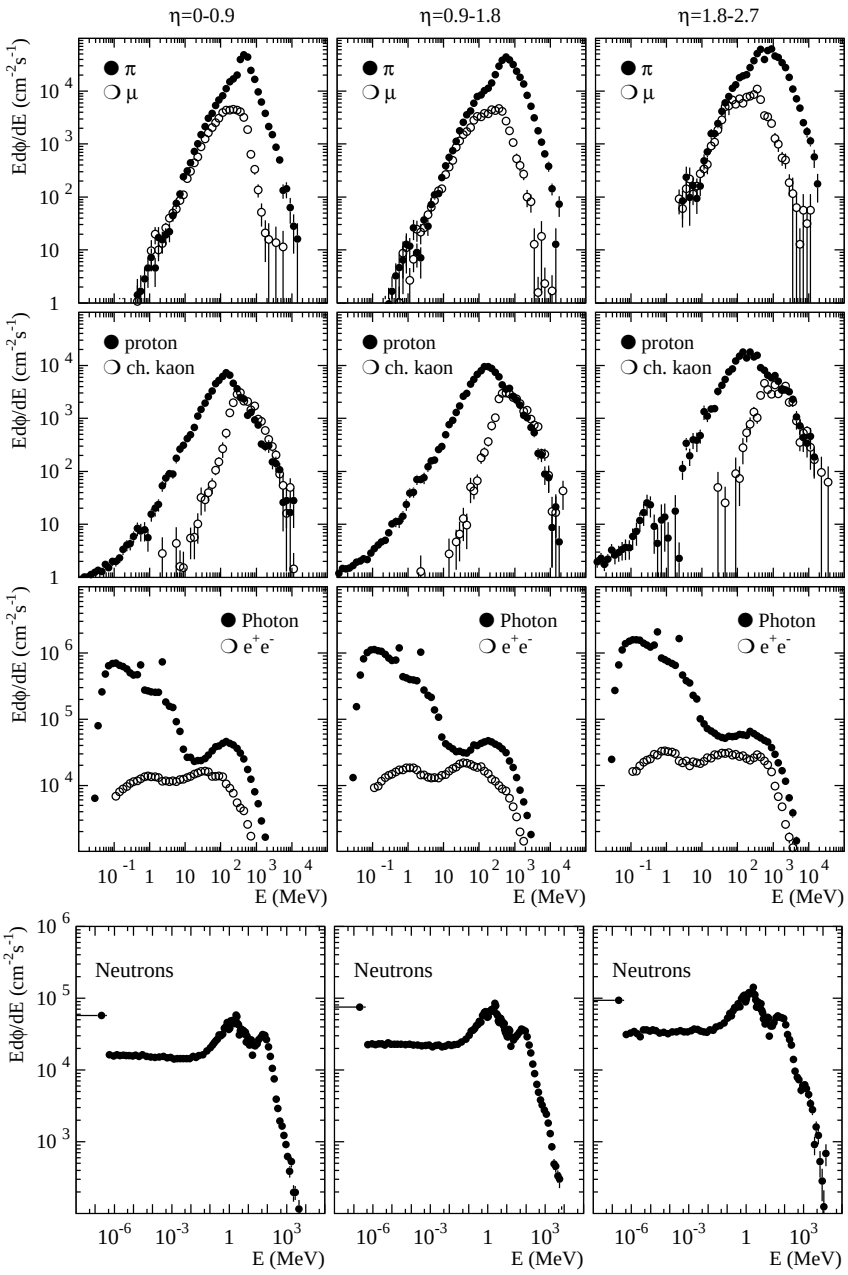


**Fig. A.8:** Energy spectra of the most important particles types in the MSGC Tracker. All values are for a luminosity of $10^{34}$ cm$^{-2}$s$^{-1}$.

### A.10.1 Highly ionizing particle rates

MSGC detectors can be susceptible to destructive sparks if the safe operational window is exceeded. In a given environment this window is bounded from below by the requirement to have sufficient efficiency for detection of minimum-ionizing particles (mip) and from above by the onset of the streamer regime.

If the cathode voltage is at the higher limit the chamber may survive perfectly well minimum ionizing tracks, but the passage of a slow heavy particle could trigger a spark.

In Ne/DME the energy loss of a minimum-ionizing particle is of the order of 400 eV/mm. Each slow heavy fragment is characterized by a maximum energy deposition occurring at a characteristic energy. At energies lower than this, the stopping power decreases. For a proton

this maximum deposition is about 300 times higher than the average deposition of a mip, but a silicon ion can reach up to $10^4$ times the mip ionization density.

Heavy recoil ions are produced at the LHC in hadronic interactions, which take place in the substrate, the drift plane, the gas or the gold strips. Detailed simulations [A-23] have shown that the gold strips play a particularly important role, since they are the origin of the most densely ionizing particles. Although most of the heavy fragments are stopped before entering the sensitive gas volume, it has been estimated that about once per minute a fragment with more than $10^4$ times the mip ionization power is observed per cm$^2$ in a MSGC at $r = 75$ cm if the LHC is operating at its peak luminosity. Figure A.9 shows the simulated spectrum of maximum energy depositions expected from inelastic hadronic interactions at the LHC. This is the dominant contribution at the highest ionization densities. Elastic interactions and neutron reactions, which are important for ionization densities below 100 keV/500 $\mu$m, reach only to a maximum deposition of about 1 MeV/500 $\mu$m [A-23]. In Fig. A.9 the fragments originating from the different parts of the MSGC are shown separately, clearly illustrating the special role of the gold strips.

It has been shown in Ref. [A-23] that the behaviour of the chambers at the LHC can be reliably tested in a low-energy (300 MeV–3 GeV) hadron beam, which produces a fragment spectrum very similar to that expected at the LHC.

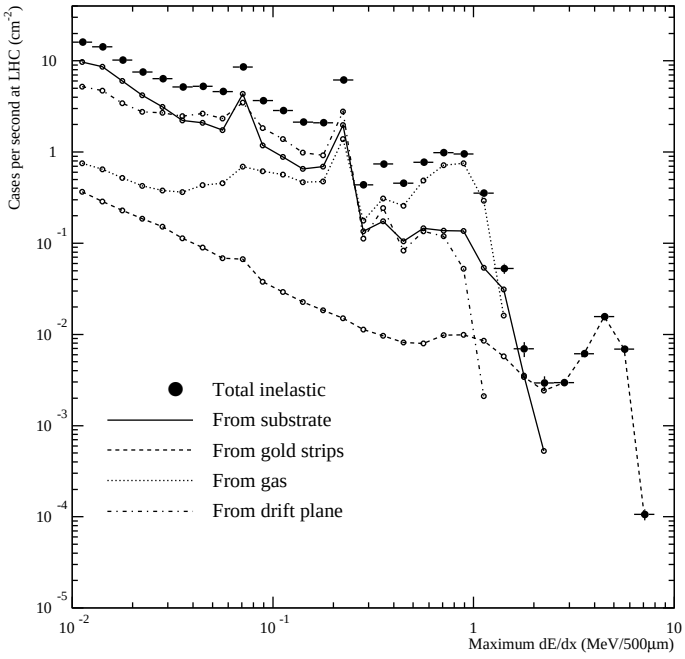


**Fig. A.9:** Probability distribution of maximum ionization densities in the MSGC gas [A-23]. The chamber is exposed to a fluence expected at a radius of 50 cm when the LHC operates at peak luminosity. The average deposition of a mip would be about 200 eV/500 $\mu$m and so would lie far left, out of the plot.

## A.11 Alignment System

The alignment system will utilize sensors for detection of laser light. These will be positioned at three different radii at the end of the Tracker. Although the small number of sensors makes a replacement feasible, it should be ensured that the radiation hardness is sufficient at least for the period between two annual shutdowns.

Table A.8 gives the dose rates and fast hadron fluences at the presently foreseen sensor positions. The dose values correspond to dose in air, but the dose in silicon is only slightly

higher. Local material concentrations close to the sensors are likely to be more significant, since they could affect the dose. The hadron fluences are not sensitive to the presence of small amounts of material.

The values of Table A.8 are given for an integrated luminosity of $5 \times 10^5$ pb$^{-1}$. According to the assumed operation schedule, the first years will remain far below the nominal luminosity but when the LHC has reached its design performance, about $0.75 \times 10^5$ pb$^{-1}$ could be accumulated per calendar year. Thus, for sensors to last from one shutdown to the next at a later phase of the LHC, they should survive at least one-sixth of the radiation doses and fluences reported in Table A.8.

**Table A.8:** Radiation dose and fast hadron fluences at the position where sensors of the alignment system are foreseen. The values correspond to an integrated luminosity of $5 \times 10^5$ pb$^{-1}$

| Radius (cm) | Dose (kGy) | $E > 100$ keV neutrons ($10^{13}$ cm$^{-2}$s$^{-1}$) | Charged hadrons ($10^{13}$ cm$^{-2}$s$^{-1}$) |
|---|---|---|---|
| 19 | 138 ± 5 | 12.3 ± 0.5 | 20.5 ± 0.4 |
| 63 | 22.3 ± 0.9 | 4.5 ± 0.1 | 1.91 ± 0.05 |
| 117 | 2.3 ± 0.2 | 2.09 ± 0.07 | 0.23 ± 0.01 |

## A.12 Beam Loss Related Contribution

Figure A.10 shows the dose, the neutron flux ($E > 100$ keV) and the charged hadron flux per proton lost on the collimator. A comparison with the fluences during pp operation shows that even a loss of $2 \times 10^{14}$ protons would expose the Tracker to only about one per cent of the total fluence expected for $5 \times 10^5$ pb$^{-1}$ of normal pp operation.

Although this shows that beam losses cannot be expected to give significant contributions to the bulk damage of the silicon detectors, this result should not be interpreted to imply that beam losses could not damage the Tracker.

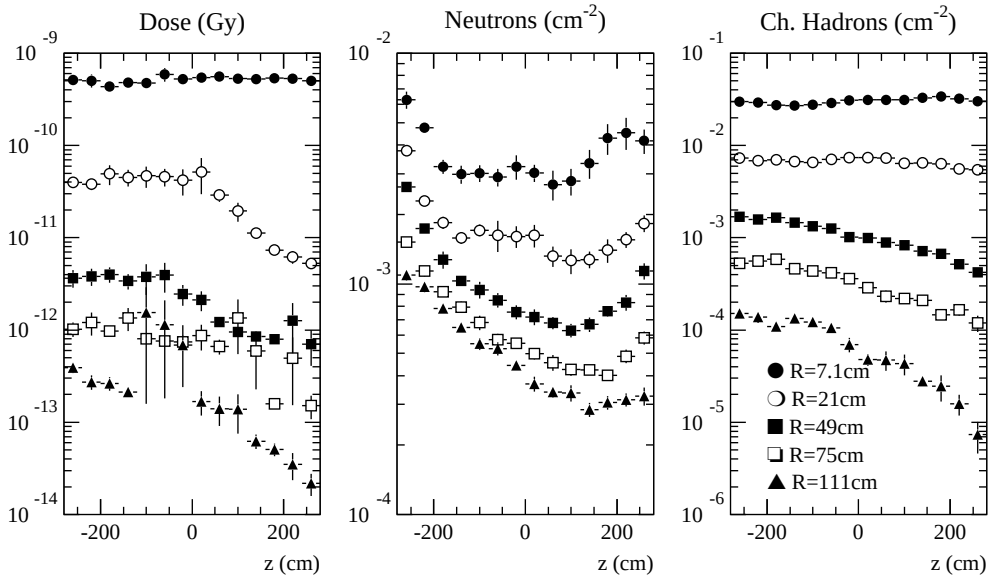


**Fig. A.10:** Absorbed dose and hadron fluxes for one 7 TeV proton lost on the collimator at positive $z$ (proton heading towards negative $z$). The explanation of symbols given in the rightmost figure applies also to the other plots.

In particular an instantaneous loss of a fraction of the beam could lead to a very high occupancy at the Tracker. This could generate pulses which permanently damage the electronics of the detectors. Assuming a beam loss duration of 1 $\mu$s, a comparison of Fig A.10 and the dose values in Table A.5 show that a loss of about 100 protons on the collimator would give an instantaneous dose comparable to normal pp operation.

As discussed in Section A.7.7 this assumption of losses on the collimator is made only to illustrate the effect of beam losses close to the experiment. A study of realistic loss patterns in accidental conditions is under way and preliminary results predict no losses on the collimator, but there is indication that significant beam losses could take place in the low-$\beta$ string. With more attenuating material between the loss point and the Tracker the effect of such losses on the Tracker would be less than the estimates in Fig. A.10 suggest. However, detailed loss information is needed before quantitative statements are possible. The present study only serves to indicate that accidental beam losses, due to the potentially high instantaneous particle rates, have to be considered in detail for the Tracker design.

## A.13 Detector Background Due to Induced Radioactivity

The motivation to consider background due to induced activity explicitly for the Tracker is that radioactive decays are not included in the standard simulation codes. Often these effects are negligible, but for the Tracker this cannot be assumed without a detailed simulation.

The reason is that photons can travel relatively large distances in the Tracker and thus give non-local effects. So a highly activated region could in principle affect the background in a lower occupancy area. For the Tracker such potential sources are the highly activated beam pipe, inner parts of the Tracker with respect to outer ones, but also the massive ECAL, surrounding the whole Tracker. The simulation of the induced-activity photon flux is described in Section A.7.8 and Ref. [A-21]. The photon flux estimates obtained in these simulations are given in Table A.9 for the barrel detector layers. For comparison the flux of photons, as given by the normal FLUKA simulations, is given for the corresponding positions.

**Table A.9:** Left: comparison of the photon flux caused by induced activity and the prompt photon flux due to the hadronic and electromagnetic cascades. The latter includes neutron capture and de-excitation photons. Right: comparison of local flux due to induced activity $\beta$-particles and the charged flux expected at the barrel layers. The values of prompt $\gamma$-fluxes and charged fluxes correspond to LHC peak luminosity, the induced activity fluxes to the end of the tenth year of operation. The values are averages over the indicated barrel layers and are given in $\mathrm{cm}^{-2}\mathrm{s}^{-1}$

| | $\gamma$-flux (ind. act.) | $\gamma$-flux (prompt) | $\beta$-flux | Charged flux |
|---|---|---|---|---|
| $r = 7.1$ cm | $9.7\times10^4$ | $4.9\times10^7$ | $4\times10^3$ | $2.4\times10^7$ |
| $r = 22$ cm | $5.8\times10^4$ | $5.9\times10^6$ | $5\times10^2$ | $3.8\times10^6$ |
| $r = 58$ cm | $3.8\times10^4$ | $3.3\times10^6$ | $8\times10^1$ | $6.9\times10^5$ |
| $r = 74.5$ cm | $3.2\times10^4$ | $2.9\times10^6$ | $1.6\times10^2$ | $3.9\times10^5$ |
| $r = 114.5$ cm | $2.3\times10^4$ | $2.2\times10^6$ | $1.4\times10^2$ | $1.2\times10^5$ |

At the pixel detector 88% of the induced-activity photon flux originates from the Tracker and beam pipe structures and 10% is due to the $^{187}$W produced in the ECAL crystals. At the outermost barrel MSGC layer 52% of the photon flux is from the Tracker structures and 40% from the $^{187}$W.

The spectrum of the induced-activity photons is very different from the prompt photon spectrum. The most important difference which can be seen in Fig. A.11 is that the high-energy component, originating mostly from $\pi^0$ decays is not present in the induced-activity spectrum.

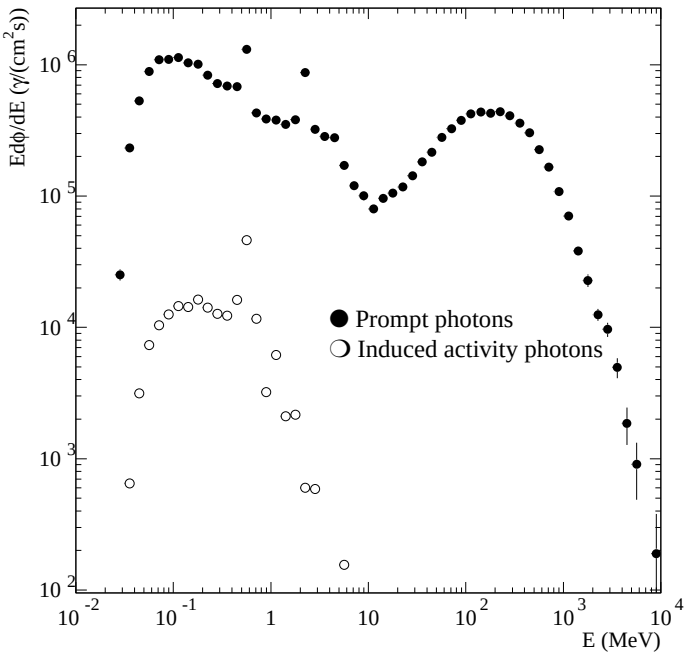


**Fig. A.11:** Energy spectra of prompt photons and induced-activity photons in the silicon Tracker in the region $|\eta|$ <0.9 between radii of 20 cm and 40 cm.

It is obvious from the values given in Table A.9 and from the spectra shown in Fig. A.11 that the photon flux from induced activity cannot significantly increase the occupancy in the Tracker.

Compared to the photons the effects of $\beta$-activity are much more local and affect the detector only at the position where the activation occurred. Since the detector elements are much thinner than a hadronic mean free path the saturation activity will locally always be a small fraction of the activating flux. Since this activating flux consists mostly of charged hadrons, this implies that local $\beta$-activity cannot form a significant fraction of the background. Services and support structures close to the detector and neutron activation can increase the ratio between $\beta$-rate and charged activating flux. Thus we provide in Table A.9 an estimate of the $\beta$-flux in barrel detectors at different radii. The values, obtained with quite pessimistic assumptions concerning services [A-21], prove that radioactive $\beta$ decays do not contribute significantly to the Tracker occupancy.